




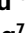

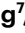



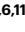
Continuous epitaxy of single-crystal graphite films by isothermal carbon diffusion through nickel

Received: 17 December 2021

Accepted: 5 September 2022

Published online: 27 October 2022

 Check for updates

Zhibin Zhang ^{1,16}, Mingchao Ding ^{2,3,16}, Ting Cheng ^{4,5,16}, Ruixi Qiao ⁶, Mengze Zhao¹, Mingyan Luo⁷, Enze Wang⁸, Yufei Sun⁸, Shuai Zhang⁹, Xingguang Li¹, Zhihong Zhang¹, Hancheng Mao¹⁰, Fang Liu ¹, Ying Fu¹¹, Kehai Liu¹¹, Dingxin Zou¹², Can Liu ¹, Muhong Wu ^{6,11,13}, Chuanlin Fan ¹⁰, Qingshan Zhu¹⁰, Xinqiang Wang ¹, Peng Gao ⁶, Qunyang Li ⁹, Kai Liu ⁸, Yuanbo Zhang⁷, Xuedong Bai ^{2,3,11}, Dapeng Yu ¹² , Feng Ding ^{4,14} , Enge Wang ^{6,11,15}  and Kaihui Liu ^{1,6,11} 

Multilayer van der Waals (vdW) film materials have attracted extensive interest from the perspective of both fundamental research^{1–3} and technology^{4–7}. However, the synthesis of large, thick, single-crystal vdW materials remains a great challenge because the lack of out-of-plane chemical bonds weakens the epitaxial relationship between neighbouring layers^{8–31}. Here we report the continuous epitaxial growth of single-crystal graphite films with thickness up to 100,000 layers on high-index, single-crystal nickel (Ni) foils. Our epitaxial graphite films demonstrate high single crystallinity, including an ultra-flat surface, centimetre-size single-crystal domains and a perfect AB-stacking structure. The exfoliated graphene shows excellent physical properties, such as a high thermal conductivity of $\sim 2,880 \text{ W m}^{-1} \text{ K}^{-1}$, intrinsic Young's modulus of $\sim 1.0 \text{ TPa}$ and low doping density of $\sim 2.2 \times 10^{10} \text{ cm}^{-2}$. The growth of each single-crystal graphene layer is realized by step edge-guided epitaxy on a high-index Ni surface, and continuous growth is enabled by the isothermal dissolution–diffusion–precipitation of carbon atoms driven by a chemical potential gradient between the two Ni surfaces. The isothermal growth enables the layers to grow at optimal conditions, without stacking disorders or stress gradients in the final graphite. Our findings provide a facile and scalable avenue for the synthesis of high-quality, thick vdW films for various applications.

In contrast to the great challenge of synthesizing single-crystal graphite, the monolayer form of graphene has been successfully produced on various substrates^{28–31}, with sizes up to the submicrometre scale. Naturally, one can suppose that high-quality, single-crystal graphite films can be obtained finally if the high-quality graphene can be continuously grown in a layer-by-layer manner, either by adding a new layer above

the preformed layers (top growth) or by growing a new layer between the preformed layers and the substrate (bottom growth). However, 'top growth' of a new graphene layer cannot be assisted by the typical substrates used, as their catalytic ability is mostly over the short range. The 'bottom growth' route has no such catalytic limitation, but requires a continuous supply of carbon atoms to the interface between

A full list of affiliations appears at the end of the paper. ✉ e-mail: yudp@sustech.edu.cn; f.ding@unist.ac.kr; egwang@pku.edu.cn; khliu@pku.edu.cn

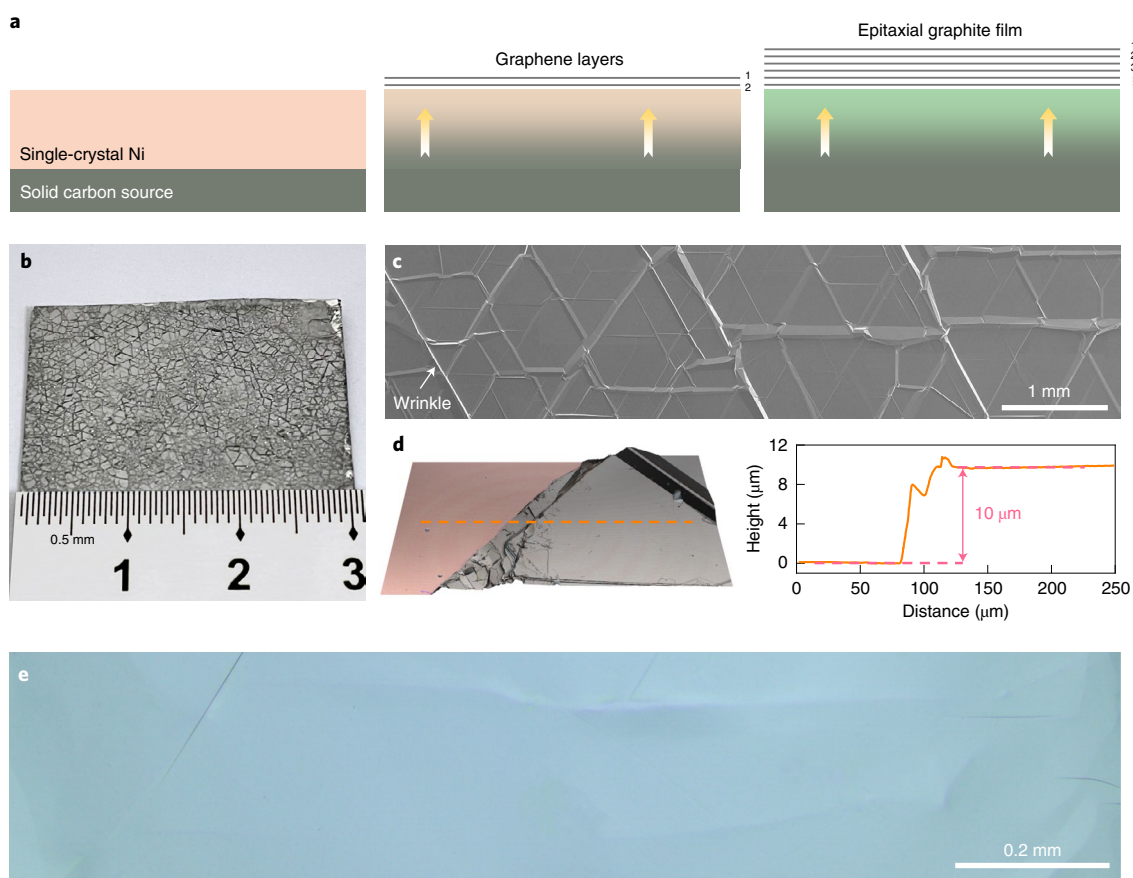


Fig. 1 | Continuous growth of the large epitaxial graphite film. **a**, Schematic illustration for the continuous growth of epitaxial graphite. Carbon atoms from the solid carbon source first dissolve into the single-crystal Ni foil (left), then diffuse to the other surface of the Ni foil to form graphene layer by layer (middle) and, finally, a large epitaxial graphite film is obtained (right). **b**, Photograph of an epitaxial graphite film with a size of $2 \times 3 \text{ cm}^2$. **c**, SEM image of the epitaxial

graphite film. Three sets of parallel wrinkles with a relative angle of 60° or 120° are observed. **d**, Thickness characterization of the epitaxial graphite film transferred onto a SiO_2/Si substrate. Left: 3D confocal micrograph of the graphite film on the substrate. Right: the height profile along the orange dashed line in the left panel. **e**, Optical image of the wrinkle-free graphite film after chlorination treatment at high temperature.

the as-grown graphite film and the substrate. Currently, there is still no effective way to realize the continuous growth of graphene layers into a high-quality, single-crystal graphite.

Here we propose a continuous epitaxial method to realize the growth of high-quality, single-crystal graphite following the ‘bottom growth’ route, in which a solid carbon source is placed on one surface of a metal foil to enable the continuous supply of carbon atoms via isothermal dissolution–diffusion–precipitation at high temperature (Fig. 1a). In this design, carbon atoms from the solid carbon source will isothermally dissolve into, and then diffuse through, the metal foil, finally precipitating on the opposite surface of the metal foil to form graphene layers continuously. In the traditional dissolution–precipitation approach, a cooling process is required to drive the graphite growth and thus the top and bottom graphene layers of the graphite must be grown at different temperatures. The variation of the temperature during growth does not allow each graphene layer to be grown at the same optimal temperature and results in contraction of the substrate. Both variation of the growth temperature from the optimal one and contraction of the substrate may lead to inevitable disorders and stress gradients in the final graphite. On the other hand, the proposed isothermal dissolution–diffusion–precipitation method used in our experiment ensures that the growth of every graphene layer is at the optimal temperature and under well-optimized conditions, finally leading to high-quality, single-crystal graphite films.

After careful investigation, we chose Ni rather than other metals as the substrate, for the following reasons: (1) Ni has a high carbon solubility ($\sim 2.2 \times 10^{21}$ carbon atoms per cm^3 at $1,300^\circ\text{C}$) and a large carbon diffusivity (the diffusion length can be $\sim 100 \mu\text{m}$ at $1,300^\circ\text{C}$) (ref. ²²), both of which are critical to guarantee the adequate and continuous supply of carbon atoms (Supplementary Fig. 1a); (2) centimetre-scale, single-crystal Ni foils with different surface indices can be produced from commercial foil products using our recently developed seeded growth technique³², which will benefit the homogeneous growth of large-scale, high-quality graphite films (Supplementary Fig. 1b); and (3) the step edges of the high-index, single-crystal Ni foils can robustly facilitate the quick nucleation and fast epitaxial growth of graphene at the interface between the preformed graphite and the substrate in practice (Supplementary Figs. 1c–e and 2).

In our experiment, the single-crystal Ni foil (with typical thickness of $100 \mu\text{m}$) was pressed against the solid carbon source (such as graphite paper) to achieve an intimate contact. The growth was performed at $1,300^\circ\text{C}$, followed by an ultra-slow cooling process (Supplementary Fig. 3). As a result, a homogeneous epitaxial graphite film with a size of $2 \times 3 \text{ cm}^2$ was successfully synthesized (Fig. 1b,c). The thickness of this film was measured by confocal microscopy and found to be about $10 \mu\text{m}$ (Fig. 1d) after being transferred onto a SiO_2/Si substrate, which is hundreds of times thicker than has been reported in the recent literature^{26,27}. Wrinkles with heights of $0.1\text{--}2 \mu\text{m}$ formed during the cooling process after the growth, as Ni will contract by 2.3% more than graphite

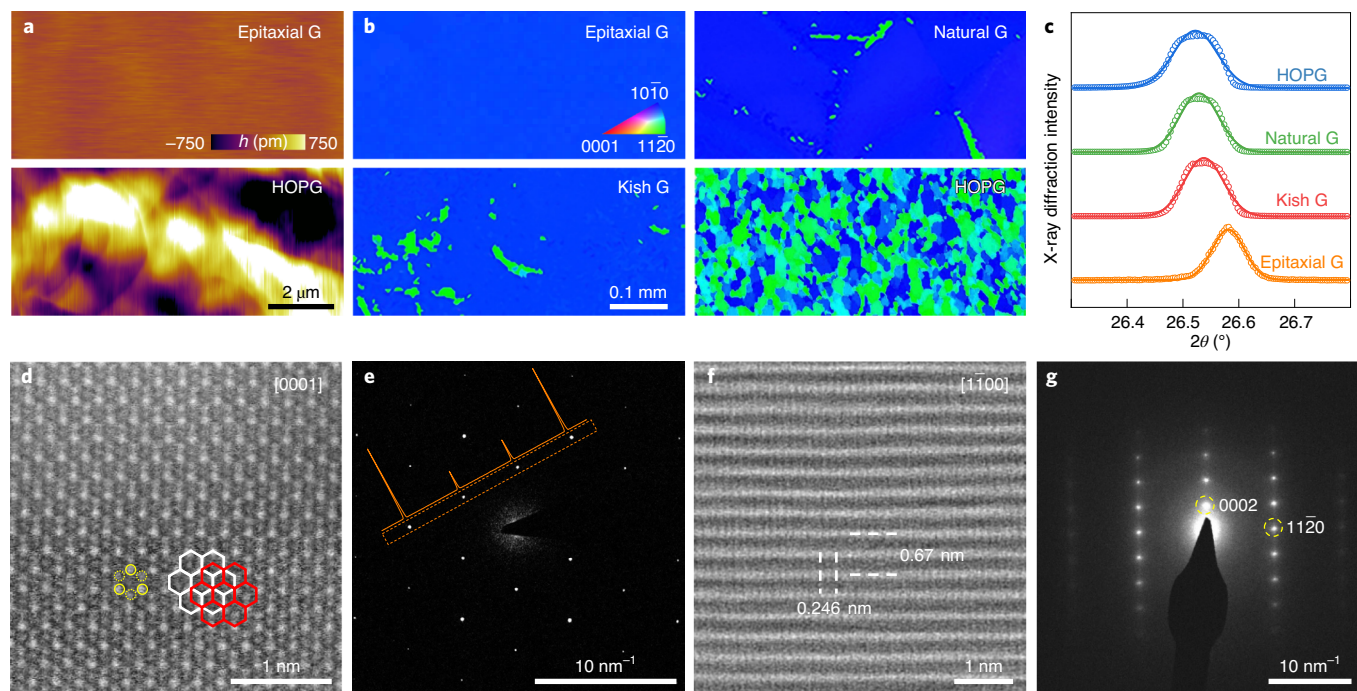


Fig. 2 | Structural characterization of the epitaxial graphite film. **a**, AFM roughness (standard deviation of the height, h) images of epitaxial graphite (G) and HOPG. The measured roughness is 25 pm and 600 pm for epitaxial graphite and HOPG, respectively. **b**, EBSD IPF-y maps of epitaxial graphite, kish graphite, natural graphite and HOPG. For kish graphite, natural graphite and HOPG, the IPF-y images show spotted and even colourful patterns, indicating the typical small domain size of $\sim 100 \mu\text{m}$ in these graphitic materials. **c**, X-ray diffraction 2θ scan spectra of the four kinds of graphite samples, where a larger 2θ value

indicates a smaller interlayer distance. **d, e**, Atomically resolved STEM image of the epitaxial graphite film (**d**) and its corresponding SAED pattern (**e**). The white and red hexagons correspond to the odd and even graphene layers, and the yellow circles (solid circles, overlapped carbon atoms with brighter contrast; dashed circles, suspended carbon atoms with darker contrast) demonstrate the AB-stacking structure of the graphite film. The orange line in **e** is the intensity profile along the dashed box. **f, g**, Cross-sectional, atomically resolved STEM image (**f**) of the epitaxial graphite film and its corresponding SAED pattern (**g**).

when the temperature drops from 1,300 °C to 20 °C (ref. ³³). Regions away from the wrinkles are extremely flat, with a roughness of $<30 \text{ pm}$ and even atomic steps are not observed in all the measured samples. In contrast, highly oriented pyrolytic graphite (HOPG), widely used as a standard calibration sample in surface science, has a roughness of $\sim 600 \text{ pm}$ with distinguishable grain tilts and steps (Fig. 2a and Supplementary Fig. 4).

Systematic characterizations reveal that the as-grown epitaxial graphite film has the highest single-crystalline quality amongst all the well-known graphitic materials, including natural graphite, kish graphite and HOPG (Supplementary Table 1). The large-scale single crystallinity can be directly deduced from the wrinkle characteristics first. Due to the intrinsic C_{3v} lattice symmetry, graphite film shrinks and tends to form wrinkles along three main armchair directions³³. In a single-crystal graphite film, these wrinkles should have three sets of parallel directions, with a relative angle of 60° or 120°, as observed in the scanning electron microscopy (SEM) image of our epitaxial graphite film (Fig. 1c). The atom-resolved atomic force microscopy (AFM) images (Supplementary Fig. 5) confirm that the obtained graphite holds the same hexagonal lattice when crossing a wrinkle and remains a single crystal. These wrinkles could be eliminated by etching the Ni foil away at high temperatures. Similarly to the industrial purification procedure of graphite and recent work on eliminating wrinkles^{10,34}, we used chlorine gas (Cl_2) to remove the Ni substrate after the graphite growth and finally obtained millimetre-scale, wrinkle-free, single-crystal graphite samples (Fig. 1e). The uniform colour in the y direction of the inverse pole figure (IPF y) in the electron back-scattered diffraction (EBSD) mappings further confirmed that our graphite film is indeed a single crystal with a size up to centimetre scale (Fig. 2b and Supplementary Fig. 6).

The interlayer crystal structure of the epitaxial graphite film was evaluated by high-resolution X-ray diffraction. Quite strikingly, our as-grown graphite film shows the largest (0002) peak at a 2θ of $\sim 26.58^\circ$ (Fig. 2c), which corresponds to an interlayer distance of 0.3353 nm, approaching the theoretical value closely¹². X-ray diffraction ϕ scan was further performed, and the perfect six-fold pattern was obtained (Supplementary Fig. 7), indicating the intrinsic symmetry of the large single-crystal graphite. Further atomically resolved scanning transmission electron microscopy (STEM) and selected area electron diffraction (SAED) results reveal that the adjacent layers are in a perfect AB-stacking structure (Fig. 2d,e), where three atoms with brighter contrast are observed in the STEM image and the outer and inner diffraction spots in the SAED patterns have an intensity ratio of more than 2. The stacking structure was also visualized and confirmed by the cross-sectional STEM image and corresponding SAED pattern with the a -axis and c -axis lattice constants measured as 0.246 nm and 0.670 nm, respectively (Fig. 2f,g).

To further evaluate the crystal quality of the epitaxial graphite film, we exfoliated it into monolayer or few-layer graphene and investigated the thermal, mechanical and electronic properties (Fig. 3a and Supplementary Fig. 8). The Raman optothermal measurements on exfoliated films show that our graphite film has a thermal conductivity of $2,880 \pm 90 \text{ W m}^{-1} \text{ K}^{-1}$ (Supplementary Fig. 9a–d). This value is the highest amongst all the graphite films measured in this work and others reported in previous works^{35,36} (Fig. 3b and Supplementary Table 2). The two-dimensional (2D) Young's modulus of monolayer graphene obtained by 15 nano-indentation tests was $346 \pm 20 \text{ N m}^{-1}$, corresponding to the three-dimensional (3D) Young's modulus of $1.03 \pm 0.06 \text{ TPa}$ (Fig. 3c and Supplementary Fig. 9e), which is consistent with the theoretical limit^{37,38}.

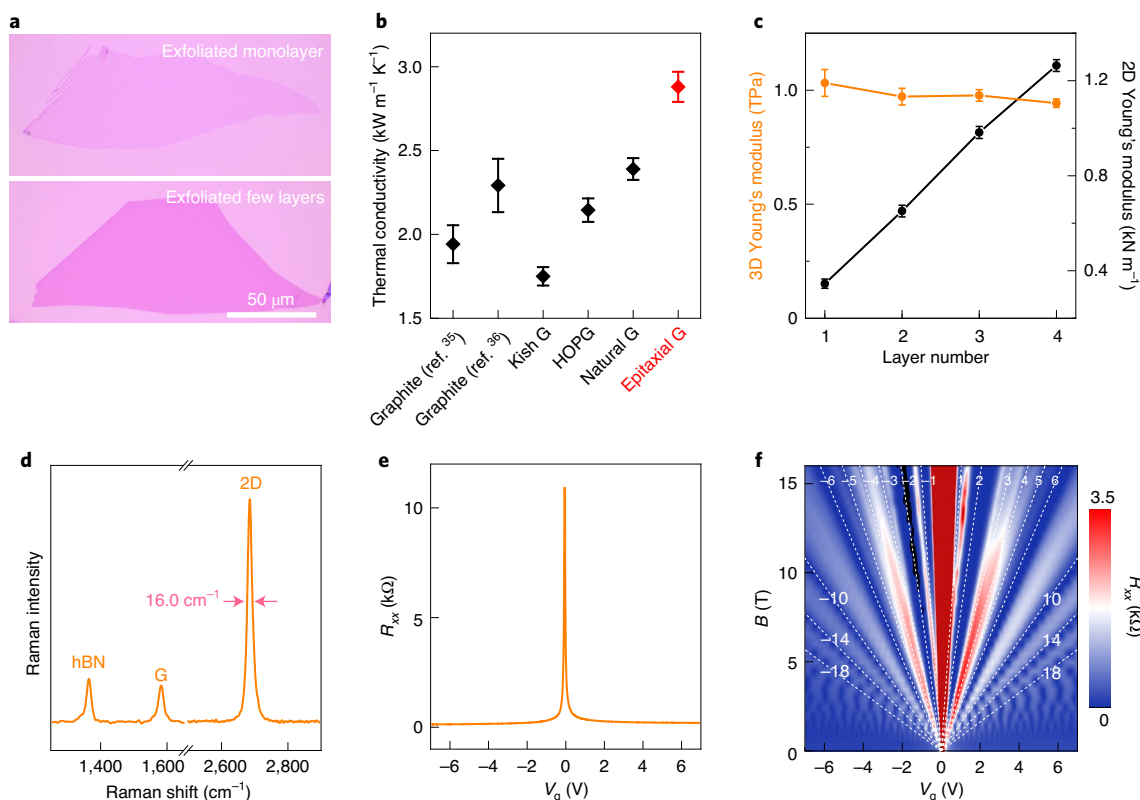


Fig. 3 | Thermal, mechanical and electronic properties of the exfoliated graphene monolayer and few layers. **a**, Optical image of the exfoliated monolayer and few-layer graphene from the epitaxial graphite film. **b**, Comparison of the thermal conductivity of different kinds of graphite. The first two values are from the literature, and the last four data values were measured in our experiments using the Raman optothermal technique. Thermal conductivity of the epitaxial graphite film was calculated as $2,880 \pm 90 \text{ W m}^{-1} \text{ K}^{-1}$.

Error bars indicate \pm s.d. **c**, Two-dimensional and 3D Young's modulus of the exfoliated graphene films with different layer numbers. Error bars indicate \pm s.d. **d**, Raman spectrum of the hBN/graphene/hBN heterostructure, with a very narrow 2D FWHM observed. **e**, Resistance (R_{xx}) as a function of applied back-gate voltage (V_g) at $T = 1.5 \text{ K}$ and $B = 0 \text{ T}$. **f**, Landau fan diagram of R_{xx} of graphene as a function of both V_g and perpendicular magnetic field B , with B ranging up to 16 T.

The quality of the epitaxial graphite film was further evaluated for its monolayer encapsulated with hexagonal boron nitride (hBN) flakes³⁹. A very small full-width at half-maximum (FWHM, $\sim 16 \text{ cm}^{-1}$) of the Raman 2D peak (Fig. 3d) was obtained. Such a low value is attributed to the uniform strain distribution, low carrier doping and high purity of the graphene samples⁴⁰. Transport measurement on a graphite-gated hBN/graphene/hBN heterostructure at 1.5 K (Supplementary Fig. 10a,b) shows intrinsic electronic properties of the monolayer graphene sample, including a low initial doping level of $2.2 \times 10^{10} \text{ cm}^{-2}$ (Fig. 3e), an extremely narrow resistivity peak with a FWHM of about $2.9 \times 10^{10} \text{ cm}^{-2}$ (Supplementary Fig. 10c), a well-resolved Landau fan diagram with a series of broken-symmetry states at the lowest two Landau levels (Fig. 3f) and a high mobility of $\sim 150,000 \text{ cm}^2 \text{ V}^{-1} \text{ s}^{-1}$ at a carrier density of $2.2 \times 10^{10} \text{ cm}^{-2}$ (Supplementary Fig. 10d). All these observations indicate that the quality of our device is on par with the highest quality reported in the literature and that the device performance is mainly limited by the fabrication process rather than the intrinsic quality of the crystal.

Using the proposed growth method, we can obtain high-quality, single-crystal graphite films with an ultra-high growth rate, estimated as up to 0.3 layers per second, which is orders of magnitude quicker than that of graphene grown by the typical chemical vapour deposition (CVD) method. Thus, a new graphene layer must be formed by the seamless stitching of a large number of graphene islands. And the graphite growth is surely not driven by the prevailing dissolution–precipitation mechanism, otherwise the graphite thickness would not exceed $1 \mu\text{m}$ due to the limited solubility of carbon in Ni with thickness of $100 \mu\text{m}$ (ref. ²²). Here, as illustrated in Fig. 4a, the continuous growth mechanism

can be understood by a three-step process (that is, an isothermal dissolution–diffusion–precipitation process): (1) carbon atoms of the solid carbon sources have a relatively high chemical potential to dissolve into the Ni foil after overcoming a dissolution barrier (step I, the barrier is estimated at about 1.5–2 eV according to our calculations; Methods and Supplementary Fig. 11); (2) the dissolved carbon atoms diffuse through the Ni foil (step II); and (3) the dissolved carbon atoms precipitate out, grow into multiple graphene islands and these graphene islands merge into a new graphene layer at the interface between the preformed graphite and the Ni foil (step III, the barrier of graphene growth is about 2–3 eV (ref. ⁴¹)).

Quantitatively, the growth rate R of the epitaxial graphite film can be estimated as

$$R = J\nu_0, \quad (1)$$

where J is the flux of carbon atoms through the Ni foil and $\nu_0 = 8.79 \times 10^{-30} \text{ m}^3$ is the volume of a carbon atom in graphite. According to Fick's first law, the flux J is

$$J = -D\nabla\rho = -D\frac{\rho_L - \rho_R}{d} = -D\rho_0\frac{x}{d}, \quad (2)$$

where $D = 6.9 \times 10^{-10} \text{ m}^2 \text{ s}^{-1}$ is the diffusion coefficient of a carbon atom in Ni at $1,300 \text{ }^\circ\text{C}$, $\nabla\rho$ is the carbon concentration gradient, ρ_L and ρ_R are the carbon concentration on the left and right sides, respectively, $\rho_0 = 2.2 \times 10^{27} \text{ m}^{-3}$ is the average concentration of carbon atoms in Ni at

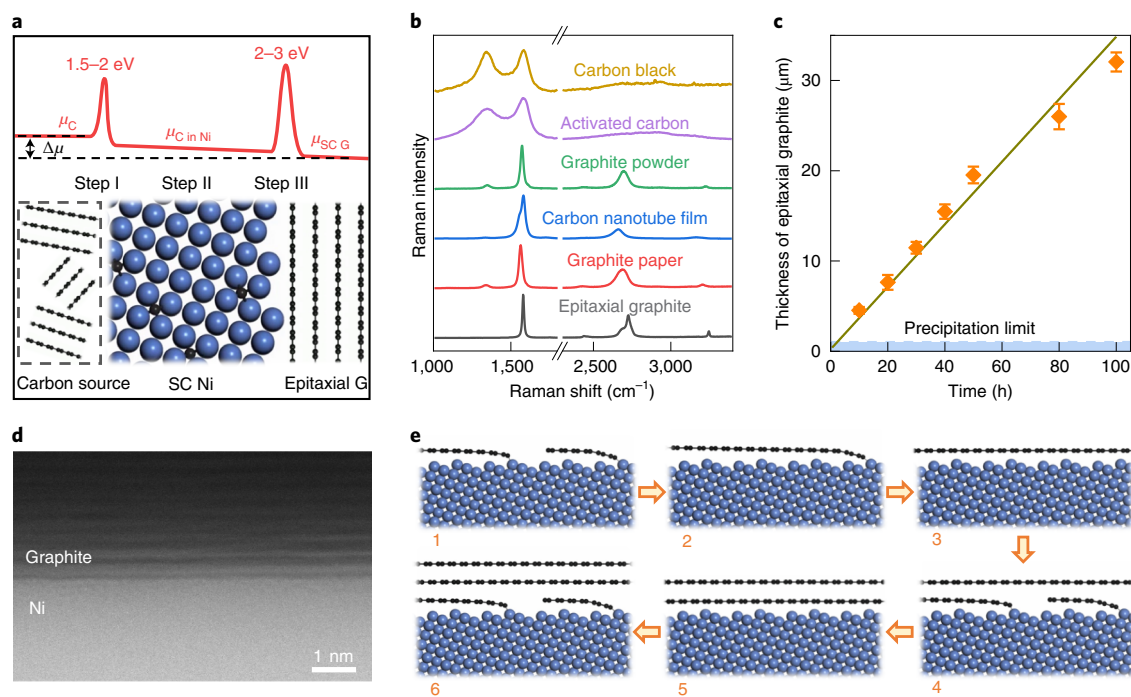


Fig. 4 | Mechanism for the continuous epitaxial growth of the graphite film.

a, Schematic diagram of the chemical potential gradient from the carbon source side to the epitaxial graphite side. The black and blue balls represent the carbon and Ni atoms, respectively, and the single-crystal Ni is noted as SC Ni. **b**, Raman spectra of epitaxial graphite and different kinds of carbon sources (carbon black, activated carbon, graphite powder, carbon nanotube film and graphite paper). All these carbon sources are successfully used for the growth of graphite film. **c**, Thickness evolution of the epitaxial graphite films with growth time (100-μm-thick Ni foil as the substrate and graphite paper as the carbon source).

The light-blue region demonstrates the graphite thickness limitation (~1 μm) in the traditional dissolution–precipitation process. Error bars indicate ± s.d.

d, Cross-sectional atomically resolved STEM image of the interface between epitaxial graphite film and the Ni surface. **e**, Schematic diagram of the epitaxial process of graphite growth on the Ni surface, where carbon atoms nucleate near step edges of the Ni surface, form graphene islands, merge into a large single-crystal monolayer seamlessly, push up the preformed graphene layers and form AB stacking between adjacent graphene layers.

1,300 °C, $d = 100 \mu\text{m}$ is the thickness of the Ni foil and $x < 1$ is a factor denoting the relative carbon concentration difference on both sides of the Ni foil. From the experimental growth rate, $R = 10^{-4} \mu\text{m s}^{-1}$, we found that the chemical potential difference ($\Delta\mu = kT \ln(1+x)$) on two sides of the Ni foil is of the order of magnitude of 0.1 meV (see Methods for more details), which can be easily realized by most solid carbon sources. Indeed, we have found that various carbon materials, such as carbon black, activated carbon, graphite powder, carbon nanotube film and graphite paper, can be used as carbon sources to grow graphite films (Fig. 4b and Supplementary Fig. 12), demonstrating that this new approach of graphite synthesis can tolerate the variation of carbon sources and the impurities in them. And, the continuous growth of graphene monolayers could finally lead to a high-quality, single-crystal graphite film with thickness up to 35 μm (more than 100,000 graphene monolayers) in 5 days (Fig. 4c).

Once the carbon atoms precipitated out driven by the chemical potential gradient, the subsequent growth of high-quality, single-crystal graphite films follows the epitaxial growth mechanism (Fig. 4d,e), and it is templated by both the step edges of the high-index Ni surface and the preformed graphite. Numerous unidirectionally aligned graphene islands nucleate at the parallel atomic step edges of the Ni surface and then merge into a large single-crystal graphene monolayer seamlessly. Then, the newly grown graphene layer forms AB stacking with the preformed graphite, as the AB-stacking configuration is the energy minimum state⁴².

We found that our graphite was also of high purity, as the atomic carbon transport through the Ni foil and the recrystallization of carbon atoms on the other surface of the Ni foil will naturally block impurities in the carbon sources (similar to solvent refining for the purification

of metal in the field of metallurgy). The obtained high-quality, epitaxial graphite films will potentially find applications in many areas, for example, in solid super lubricants as super-flat isolating layers, in circuit thermal engineering as high thermal conducting films, in acoustic devices as mechanical resonators and in advanced electrodes as electrochemical capacitors.

Online content

Any methods, additional references, Nature Research reporting summaries, source data, extended data, supplementary information, acknowledgements, peer review information; details of author contributions and competing interests; and statements of data and code availability are available at <https://doi.org/10.1038/s41565-022-01230-0>.

References

1. Cao, Y. et al. Unconventional superconductivity in magic-angle graphene superlattices. *Nature* **556**, 43–50 (2018).
2. Zhou, H. et al. Half- and quarter-metals in rhombohedral trilayer graphene. *Nature* **598**, 429–433 (2021).
3. Shi, Y. et al. Electronic phase separation in multilayer rhombohedral graphite. *Nature* **584**, 210–214 (2020).
4. Liu, Z. et al. Observation of microscale superlubricity in graphite. *Phys. Rev. Lett.* **108**, 205503 (2012).
5. Ghosh, S. et al. Dimensional crossover of thermal transport in few-layer graphene. *Nat. Mater.* **9**, 555–558 (2010).
6. Zhou, Q., Zheng, J., Onishi, S., Crommie, M. F. & Zettl, A. K. Graphene electrostatic microphone and ultrasonic radio. *Proc. Natl Acad. Sci. USA* **112**, 8942–8946 (2015).

7. El-Kady, M. F., Strong, V., Dubin, S. & Kaner, R. B. Laser scribing of high-performance and flexible graphene-based electrochemical capacitors. *Science* **335**, 1326–1330 (2012).
8. Li, P. C. Preparation of single-crystal graphite from melts. *Nature* **192**, 864–865 (1961).
9. Austerma, S. B., Myron, S. M. & Wagner, J. W. Growth and characterization of graphite single crystals. *Carbon* **5**, 551–557 (1967).
10. Inagaki, M. *New Carbons: Control of Structure and Functions* (Elsevier Science, 2000).
11. Liu, S. L. & Loper, C. R. The formation of kish graphite. *Carbon* **29**, 547–555 (1991).
12. Chung, D. D. L. Review graphite. *J. Mater. Sci.* **37**, 1475–1489 (2002).
13. Karu, A. E. & Beer, M. Pyrolytic formation of highly crystalline graphite films. *J. Appl. Phys.* **37**, 2179 (1966).
14. Presland, A. E. & Walker, P. L. Growth of single-crystal graphite by pyrolysis of acetylene over metals. *Carbon* **7**, 1–8 (1969).
15. Shelton, J. C., Patil, H. R. & Blakely, J. M. Equilibrium segregation of carbon to a nickel (111) surface: a surface phase transition. *Surf. Sci.* **43**, 493–520 (1974).
16. Derbyshire, F. J., Presland, A. E. B. & Trimm, D. L. Graphite formation by dissolution-precipitation of carbon in cobalt, nickel and iron. *Carbon* **13**, 111–113 (1975).
17. Sun, Z. Z. et al. Growth of graphene from solid carbon sources. *Nature* **468**, 549–552 (2010).
18. Wang, X. B. et al. Three-dimensional strutted graphene grown by substrate-free sugar blowing for high-power-density supercapacitors. *Nat. Commun.* **4**, 2905 (2013).
19. Lehner, B. A. E. et al. Creation of conductive graphene materials by bacterial reduction using *Shewanella oneidensis*. *ChemistryOpen* **8**, 888–895 (2019).
20. Luong, D. X. et al. Gram-scale bottom-up flash graphene synthesis. *Nature* **577**, 647–651 (2020).
21. Kim, K. S. et al. Large-scale pattern growth of graphene films for stretchable transparent electrodes. *Nature* **457**, 706–710 (2009).
22. Baraton, L. et al. On the mechanisms of precipitation of graphene on nickel thin films. *Europhys. Lett.* **96**, 46003 (2011).
23. Yan, Z. et al. Growth of bilayer graphene on insulating substrates. *ACS Nano* **5**, 8187–8192 (2011).
24. Kwak, J. et al. Near room-temperature synthesis of transfer-free graphene films. *Nat. Commun.* **3**, 645 (2012).
25. Liu, S. et al. Single-crystal growth of millimeter-sized monoisotopic hexagonal boron nitride. *Chem. Mater.* **30**, 6222–6225 (2018).
26. Deokar, G. et al. Semi-transparent graphite films growth on Ni and their double-sided polymer-free transfer. *Sci. Rep.* **10**, 14703 (2020).
27. Shi, Z. Y. et al. Vapor-liquid-solid growth of large-area multilayer hexagonal boron nitride on dielectric substrates. *Nat. Commun.* **11**, 849 (2020).
28. Lee, J. H. et al. Wafer-scale growth of single-crystal monolayer graphene on reusable hydrogen-terminated germanium. *Science* **344**, 286–289 (2014).
29. Wu, T. et al. Fast growth of inch-sized single-crystalline graphene from a controlled single nucleus on Cu–Ni alloys. *Nat. Mater.* **15**, 43–47 (2016).
30. Xu, X. Z. et al. Ultrafast epitaxial growth of metre-sized single-crystal graphene on industrial Cu foil. *Sci. Bull.* **62**, 1074–1080 (2017).
31. Lin, L. et al. Towards super-clean graphene. *Nat. Commun.* **10**, 1912 (2019).
32. Wu, M. H. et al. Seeded growth of large single-crystal copper foils with high-index facets. *Nature* **581**, 406–410 (2020).
33. Meng, L. et al. Wrinkle networks in exfoliated multilayer graphene and other layered materials. *Carbon* **156**, 24–30 (2020).
34. Chatterjee, S. et al. Synthesis of highly oriented graphite films with a low wrinkle density and near-millimeter-scale lateral grains. *Chem. Mater.* **32**, 3134–3143 (2020).
35. Peng, L. et al. Ultrahigh thermal conductive yet superflexible graphene films. *Adv. Mater.* **29**, 1700589 (2017).
36. Wang, B. et al. Ultrastiff, strong, and highly thermally conductive crystalline graphitic films with mixed stacking order. *Adv. Mater.* **31**, 1909039 (2019).
37. Lee, C., Wei, X. D., Kysar, J. W. & Hone, J. Measurement of the elastic properties and intrinsic strength of monolayer graphene. *Science* **321**, 385–388 (2008).
38. Jiang, J. W., Wang, J. S. & Li, B. W. Young's modulus of graphene: a molecular dynamics study. *Phys. Rev. B* **80**, 113405 (2009).
39. Dean, C. R. et al. Boron nitride substrates for high-quality graphene electronics. *Nat. Nanotechnol.* **5**, 722–726 (2010).
40. Banszerus, L. et al. Ultrahigh-mobility graphene devices from chemical vapor deposition on reusable copper. *Sci. Adv.* **1**, e1500222 (2015).
41. Wang, D. X., Liu, Y. F., Sun, D. Y., Yuan, Q. H. & Ding, F. Thermodynamics and kinetics of graphene growth on Ni(111) and the origin of triangular-shaped graphene islands. *J. Phys. Chem. C* **122**, 3334–3340 (2018).
42. Mostaani, E., Drummond, N. D. & Fal'ko, V. I. Quantum Monte Carlo calculation of the binding energy of bilayer graphene. *Phys. Rev. Lett.* **115**, 115501 (2015).

Publisher's note Springer Nature remains neutral with regard to jurisdictional claims in published maps and institutional affiliations.

Springer Nature or its licensor holds exclusive rights to this article under a publishing agreement with the author(s) or other rightsholder(s); author self-archiving of the accepted manuscript version of this article is solely governed by the terms of such publishing agreement and applicable law.

© The Author(s), under exclusive licence to Springer Nature Limited 2022

¹State Key Laboratory for Mesoscopic Physics, Frontiers Science Centre for Nano-optoelectronics, School of Physics, Peking University, Beijing, China.

²Beijing National Laboratory for Condensed Matter Physics, Institute of Physics, Chinese Academy of Sciences, Beijing, China. ³School of Physical

Sciences, University of Chinese Academy of Sciences, Beijing, China. ⁴Centre for Multidimensional Carbon Materials, Institute for Basic Science,

Ulsan, Korea. ⁵College of Chemistry and Molecular Engineering, Academy for Advanced Interdisciplinary Studies, Peking University, Beijing, China.

⁶International Centre for Quantum Materials, Collaborative Innovation Centre of Quantum Matter, Peking University, Beijing, China. ⁷State Key Laboratory

of Surface Physics and Department of Physics, Fudan University, Shanghai, China. ⁸State Key Laboratory of New Ceramics and Fine Processing,

School of Materials Science and Engineering, Tsinghua University, Beijing, China. ⁹State Key Laboratory of Tribology in Advanced Equipment, Applied

Mechanics Laboratory, Tsinghua University, Beijing, China. ¹⁰State Key Laboratory of Multiphase Complex Systems, Institute of Process Engineering,

Chinese Academy of Sciences, Beijing, China. ¹¹Songshan Lake Materials Laboratory, Dongguan, China. ¹²Shenzhen Institute for Quantum Science and

Engineering, Southern University of Science and Technology, Shenzhen, China. ¹³Interdisciplinary Institute of Light-Element Quantum Materials and Research Centre for Light-Element Advanced Materials, Peking University, Beijing, China. ¹⁴School of Materials Science and Engineering, Ulsan National Institute of Science and Technology, Ulsan, Korea. ¹⁵School of Physics, Liaoning University, Shenyang, China. ¹⁶These authors contributed equally: Zhibin Zhang, Mingchao Ding, Ting Cheng. ✉ e-mail: yudp@sustech.edu.cn; f.ding@unist.ac.kr; egwang@pku.edu.cn; khliu@pku.edu.cn

Methods

Growth of the epitaxial graphite film

Single-crystal Ni foils with different facets (99.994%, Zhongke Crystal Materials) were placed on the surface of a solid carbon source (graphite paper, JL-AQC-5C, 99.9%, Beijing Jinglong Special Carbon Technology; carbon nanotube film, A60693, 3AChem; graphite powder, 10130, 75–82%, Alfa Aesar; activated carbon, R019801, Rhawn; and carbon black, R051937, Rhawn) on an alumina substrate and loaded into a CVD furnace (Tianjin Kaiheng, custom designed). Then, the furnace was heated to 1,300 °C in 2 h and the temperature was maintained for 1–120 h to grow graphite. After the growth, the system was slowly cooled down to room temperature (2 °C min⁻¹) to approach the isothermal state, ensuring growth with few or no disorders and defects even during the cooling process. Throughout the growth experiment, 800 standard cubic centimetres per minute (sccm) Ar and 50 sccm H₂ flowed through the tube furnace.

Chlorination treatment of the samples

The as-grown graphite film was sent into the chlorination instrument, and when the system reached 1,000 °C, Cl₂ (150 sccm) was introduced for 2 h to etch the Ni foil away. After the etching, Cl₂ was turned off and the system was held for about 30 min to pump out the Cl₂, and then the system naturally cooled down to room temperature to obtain the graphite without wrinkles.

Transfer of the epitaxial graphite film

For the wet transfer method, the obtained graphite/Ni sample was etched in FeCl₃ solution to remove the Ni, then the obtained graphite film was rinsed with deionized water several times and, finally, it was placed on the desired SiO₂/Si substrate. In addition, a modified dry transfer technique using polypropylene carbonate (PPC) was carried out to fabricate the heterostructure. The PPC film was used to pick up the hBN flake (exfoliated from hBN bulk crystals, Shanghai Onway Technology), graphene (exfoliated from our graphite) and the hBN flake under 40 °C, in sequence. Afterwards, the sample was released on graphite (exfoliated from our graphite) with SiO₂/Si substrate at 130 °C.

Measurement of the thermal conductivity of epitaxial graphite film

Thermal conductivity of the graphite film was measured using the Raman optothermal technique. Different kinds of graphite, including the epitaxial graphite obtained in this work, natural graphite (Graphenium Flakes 25–30 mm, NGS Naturgraphit), kish graphite (Grade 300, Graphene Supermarket) and HOPG (ZYA grade, NT-MDT), were exfoliated onto the holey SiO₂/Si substrate (5 μm in diameter and 300 nm in depth). The power-dependent (the relationship between laser power (*P*) and the measured Raman shift (ω)) and temperature-dependent (the relationship between *T* and ω) Raman measurements were performed. Combining the two fitting results, a thermal parameter ($\frac{\partial T}{\partial P} = \frac{\partial T}{\partial \omega} \frac{\partial \omega}{\partial P}$) was introduced to indicate the heat diffusion process. Then, we used the COMSOL Multiphysics software to simulate the experimental process. Thermal conductivity of the graphite film can be extracted by applying the experimental parameter ($\frac{\partial T}{\partial P}$) into the simulation plot.

Measurement of the Young's modulus

The epitaxial graphite film was mechanically exfoliated into graphene films with white tape (3M Scotch) onto a holey substrate with arrays of circular holes (1.5 μm or 2.0 μm in diameter and 300 nm in depth). After the sample was scanned by an AFM (Bruker Multimode 8) a few times until the image was stabilized, the sample stage was moved upwards with a distance of *z*, so that the AFM tip could apply a force *F* on the graphene film. The deformation δ of the sample can be calculated as $\delta = z - F/k$, where *k* is the spring constant of the probe, which was calibrated by the Sader method (online calibration) following a simple

harmonic oscillation model. After deducing δ , the 2D Young's modulus E^{2D} could be obtained by fitting the *F*– δ curve. The 3D Young's modulus E^{3D} was calculated by dividing E^{2D} by the sample thickness.

Device fabrication and transport measurement

We used the typical dry transfer method mentioned above to assemble the hBN/graphene/hBN/graphite heterostructure. Then, a Hall-bar-shaped mask was defined on the top hBN surface by electron-beam lithography of a polymethyl methacrylate resist, and the top BN outside the mask was etched by reactive ion etching (CHF₃:O₂ = 40:6) to expose the graphene edge. Finally, we deposited metal leads (3 nm Cr/130 nm Au) by electron-beam evaporation to make an electrical contact. After that, four-terminal transport measurements were performed using a lock-in amplifier at 13.132 Hz with a 100 nA current excitation. The sample was measured in a 16 T superconducting magnet system at a temperature of 1.5 K.

Characterization

Optical images were obtained using an Olympus BX51 microscope. SEM images were obtained using an FEI Nova NanoSEM 430 scanning electron microscope. Thickness of the graphite films was measured by a 3D laser scanning confocal microscope (KETENCE, VK-X1000). AFM images were acquired using an Asylum Research Cypher system. EBSD characterizations were carried out using a PHI 710 scanning Auger nanoprobe instrument. X-ray diffraction 2θ scan measurements were conducted using a Bruker D8 Discover system. X-ray diffraction ϕ scan measurements were performed using an X'Pert³ MRD system with a CuK α_1 X-ray source. Raman spectra were performed using a WITec alpha300R system with a laser excitation wavelength of 514 nm. STEM and SAED experiments were performed in an FEI Titan Themis G2 300 operated at 300 kV.

Calculation details

The computational results presented in this work were carried out using the density functional theory as implemented in the Vienna Ab-initio Simulation Package^{43,44}. We adopted the Perdew–Burke–Ernzerhof functional with the generalized gradient approximation to treat the exchange-correlation functional⁴⁵. For the calculation of reaction barrier and geometry relaxation, we used a kinetic energy cutoff of 400 eV and a threshold convergence of 10⁻⁵ eV and 0.01 eV Å⁻¹ for the energies and forces of the system, respectively. The energy barrier of each reaction was calculated using the climbing image nudged elastic band method⁴⁶.

To present the solid carbon source, we used a vertically aligned graphene nanoribbon (7.45 × 10.88 Å², with the edge terminated by H atoms) and attached it to the step of the single-crystal Ni surface (a step along the <110> direction was used here, with the unit cell size of 7.45 × 6.30 × 32 Å³, and the bottom two layers of the Ni atoms were fixed to represent the Ni foil). The Monkhorst–Pack *k*-point mesh of 5 × 5 × 1 was adopted. The whole carbon-dissolved process (step I in Fig. 4) was divided into two stages (Supplementary Fig. 11). First, one carbon atom detached from the edge of the carbon source to the subsurface of Ni, and then, subsequently, another carbon atom near the first dissolved carbon atom detached to the subsurface of Ni.

Estimation of the growth rate of the graphite film

Generally, the solubility of carbon in Ni is 0.53 g per 100 g at 1,300 °C (ref. 47), thus the average concentration ρ_0 of carbon atoms in Ni could be estimated as:

$$\rho_0 = 0.53\% \frac{m_{\text{Ni}}}{m_{\text{C}}} \frac{\rho_{\text{Ni}}}{m_{\text{Ni}}} N_{\text{A}} = 2.2 \times 10^{27} \text{ atoms m}^{-3} \quad (3)$$

where $m_{\text{Ni}} = 58.7$ AMU, $m_{\text{C}} = 12$ AMU, ρ_{Ni} is the density of bulk Ni of about 8.2 g cm⁻³ at 1,300 °C and N_{A} is the Avogadro constant.

The volume of a carbon atom in graphite is estimated by:

$$v_0 = \frac{m_C}{\rho_{\text{graphite}} N_A} = 8.79 \times 10^{-30} \text{ m}^3, \quad (4)$$

where the density of graphite ρ_{graphite} is about 2.266 g cm^{-3} .

By combining equations (1) and (2), the vertical growth rate of graphite is given by:

$$R = -Dv_0\rho_0 \frac{x}{d} = 0.133x \text{ } \mu\text{m s}^{-1}. \quad (5)$$

From the experimental growth rate $R = 10^{-4} \text{ } \mu\text{m s}^{-1}$, we can estimate the carbon concentration difference on both sides of the Ni foils as only $x = 0.07\%$. To obtain such a concentration gradient, the required chemical potential difference is estimated as $\Delta\mu = kT\ln(1+x) \approx 0.1 \text{ meV}$, where k is the Boltzmann constant and T is the growth temperature.

Data availability

Source data are provided with this paper. The data that support the findings of this study are available within the paper and Supplementary Information. Additional data are available from the corresponding authors upon reasonable request.

References

43. Kresse, G. & Furthmuller, J. Efficient iterative schemes for ab initio total-energy calculations using a plane-wave basis set. *Phys. Rev. B* **54**, 11169–11186 (1996).
44. Kresse, G. & Furthmuller, J. Efficiency of ab initio total-energy calculations for metals and semiconductors using a plane-wave basis set. *Comput. Mater. Sci.* **6**, 15–50 (1996).
45. Perdew, J. P., Burke, K. & Ernzerhof, M. Generalized gradient approximation made simple. *Phys. Rev. Lett.* **77**, 3865–3868 (1996).
46. Henkelman, G., Uberuaga, B. P. & Jonsson, H. A climbing image nudged elastic band method for finding saddle points and minimum energy paths. *J. Chem. Phys.* **113**, 9901–9904 (2000).
47. Lander, J. J., Kern, H. E. & Beach, A. L. Solubility and diffusion coefficient of carbon in nickel: reaction rates of nickel–carbon alloys with barium oxide. *J. Appl. Phys.* **23**, 1305–1309 (1952).

Acknowledgements

This work was supported by Guangdong Major Project of Basic and Applied Basic Research (2021B0301030002 (Engge Wang and Kaihui Liu)), the National Natural Science Foundation of China (52025023

(Kaihui Liu), 51991342 (Kaihui Liu), 52021006 (Kaihui Liu), 11888101 (Engge Wang), 92163206 (M.W.), 52172035 (M.W.), 52125307 (P.G.) and T2188101 (Kaihui Liu)), the Key R&D Programme of Guangdong Province (2019B010931001 (Kaihui Liu) and 2018B030327001 (D.Y.)), the National Key R&D Programme of China (2021YFB3200303 (Kaihui Liu), 2021YFA1400502 (M.W.)), the Strategic Priority Research Programme of Chinese Academy of Sciences (XDB33000000 (Kaihui Liu)), Beijing Natural Science Foundation (JQ19004 (Kaihui Liu)), the Tencent Foundation through the XPLOER PRIZE (Kaihui Liu) and the Institute for Basic Science of South Korea (IBS-R019-D1 (F.D.)). We acknowledge the use of the IBS-CMCM high-performance computing system simulator.

Author contributions

Kaihui Liu and Engge Wang supervised the project. Kaihui Liu conceived the experiments. F.D., Engge Wang and Kaihui Liu developed the growth mechanism. D.Y. organized the structural characterization. Zhibin Zhang and M.D. synthesized the epitaxial graphite film. T.C. and F.D. performed the theoretical analysis. X.B., Zhibin Zhang, R.Q., M.Z., X.L., F.L., Zhihong Zhang, D.Z., C.L., M.W., X.W. and P.G. performed the SEM, TEM, EBSD and X-ray diffraction experiments. Zhibin Zhang, M.D., Y.F. and Kehai Liu performed the thermal conductivity measurements. Kai Liu, Q.L., Enze Wang, Y.S. and S.Z. performed the mechanical experiments. Y.Z. and M.L. performed the electronic transport experiment. Q.Z., Zhibin Zhang, H.M. and C.F. performed the chlorination experiment. All authors discussed the results and contributed to writing the paper.

Competing interests

The authors declare no competing interests.

Additional information

Supplementary information The online version contains supplementary material available at <https://doi.org/10.1038/s41565-022-01230-0>.

Correspondence and requests for materials should be addressed to Dapeng Yu, Feng Ding, Engge Wang or Kaihui Liu.

Peer review information *Nature Nanotechnology* thanks Maria Losurdo and the other, anonymous, reviewer(s) for their contribution to the peer review of this work.

Reprints and permissions information is available at www.nature.com/reprints.